

SOFT X-RAY ABSORPTION BY Fe^{0+} TO Fe^{15+} IN ACTIVE GALACTIC NUCLEI

EHUD BEHAR,¹ MASAO SAKO,¹ AND STEVEN M. KAHN¹

Received 2001 July 7; accepted 2001 August 22

ABSTRACT

A full set of calculations is presented for inner-shell $n = 2-3$ photoexcitation of the 16 iron charge states: Fe^{0+} (Fe I) through Fe^{15+} (Fe XVI). The blend of the numerous absorption lines arising from these excitations (mainly $2p-3d$) forms an unresolved transition array (UTA), which has been recently identified as a prominent feature between 16 and 17 Å in the soft X-ray spectra of active galactic nuclei (AGNs). Despite the blending within charge states, the ample separation between the individual-ion features enables precise diagnostics of the ionization range in the absorbing medium. Column density and turbulent velocity diagnostics are also possible, albeit to a lesser accuracy. An abbreviated set of atomic parameters useful for modeling the Fe $2p-3d$ UTA is given. It is shown that the effects of accompanying photoexcitation to higher levels ($n \geq 4$), as well as the associated photoionization edges, may also be relevant to AGN spectra.

Subject headings: atomic data — atomic processes — galaxies: active — galaxies: nuclei — line: formation — X-rays: galaxies

1. INTRODUCTION

Active galactic nuclei (AGNs) viewed directly toward a supermassive black hole (e.g., Seyfert 1 galaxies) can produce a rich absorption spectrum. High-flux X-ray and UV continuum emission from the central source ionizes the ambient gas to high charge states. Consequently, the ionized gas along the line of sight imposes absorption features on the observed continuum. Away from the central source, the ionizing flux gradually diminishes, limiting the maximum charge states that can be formed, especially for high- Z elements. Nevertheless, the photon energy distribution, generally a power law, allows for a substantial fraction of energetic photons. Therefore, the intermediately ionized ions are exposed to X-ray photons that can be appreciably more energetic than the typical energies for ionization or excitation from the valence shells of these ions. When the column density through this gas is sufficient, absorption by means of inner-shell photoexcitation processes plays an important role in the formation of discrete features in the spectrum.

In particular, the $n = 2-3$ absorption lines (n being the principal quantum number of the active electron) of the cosmically abundant element iron (Fe) fall in the soft X-ray band that can be readily measured by the grating spectrometers on board *Chandra* and *XMM-Newton*. The $n = 2-3$ valence transitions are well known in the soft X-ray band for the (L-shell) ions Fe^{16+} to Fe^{23+} . The analogous, but inner-shell, excitations in Fe^{0+} to Fe^{15+} (referred to hereafter in shorthand as Fe M-shell ions) have not been given the same attention. In the laboratory, Chenais-Popovics et al. (2001) studied the opacity of a thin, laser heated Fe foil illuminated by a strong X-ray backlighter. They detected unresolved inner-shell $n = 2-3$ photoabsorption by Fe^{4+} to Fe^{9+} around 17 Å and modeled it assuming local thermodynamic equilibrium. Recently, we have reported the first astrophysical detection of a similar feature in the spectrum of the luminous quasar IRAS 13349 + 2438 (Sako et al. 2001) obtained with the Reflection Grating Spectrometer

(RGS) on board *XMM-Newton*. In that spectrum, we ascribe the broad absorption trough between 16–17 Å to an unresolved transition array (UTA) of inner-shell $n = 2-3$ (mainly $2p-3d$) lines pertaining to various Fe ions. As shown in Sako et al. (2001), the exact shape of this absorption feature is well fitted by a superposition of lines from Fe^{6+} to Fe^{11+} with ionic column densities of $(0.9-6.4) \times 10^{16} \text{ cm}^{-2}$, which correspond roughly to column densities of hydrogen atoms of a few times 10^{21} cm^{-2} . Recently, the soft X-ray spectrum of the Seyfert 1 galaxy NGC 3783 obtained with the RGS has revealed a similar, but even more prominent, Fe $2p-3d$ UTA (J. Blustin et al. 2001, in preparation). This feature, unaccounted for in the model for the *Chandra* spectrum of NGC 3783 (Kaspi et al. 2000, 2001), could explain the discrepancies between the data and the model around 17 Å in that work. A much weaker Fe $2p-3d$ UTA was tentatively identified in the Seyfert 1 galaxy Markarian 509 by Pounds et al. (2001). Figure 1 shows the Fe $2p-3d$ UTA region of the RGS spectrum for both IRAS 13349 + 2438 and NGC 3783. Despite the apparent difference in absolute flux, the shape and structure of the UTA are somewhat similar, covering approximately the same range of ionization. The transmission in NGC 3783 is evidently lower.

For both IRAS 13349 + 2438 and NGC 3783, as well as for other AGNs, the Fe $2p-3d$ UTA can be used to diagnose the ionization state and column density for the relatively low ionization components of the soft X-ray-absorbing gas. Since the Fe M-shell ions also absorb in the UV and EUV bands, they can be used to relate the UV absorber with the X-ray absorber, which have curiously shown different column densities for many sources. Additionally, the same charge states that produce the Fe $2p-3d$ UTA absorption also produce strong emission lines in the various optical bands. If both features are observed simultaneously, the Fe $2p-3d$ UTA can potentially provide an independent probe of the level of ionization in the optically emitting gas. Furthermore, if the low-ionization Fe M-shell gas is associated with the ionized skin of the putative AGN torus, as postulated by Sako et al. (2001), it can provide a constraint on the size of the torus and the inclination angle of the (host) galactic plane with respect to our line of sight.

¹ Columbia Astrophysics Laboratory and Department of Physics, Columbia University, 550 West 120th Street, New York, NY 10027; behar@astro.columbia.edu, masao@astro.columbia.edu, skahn@astro.columbia.edu.

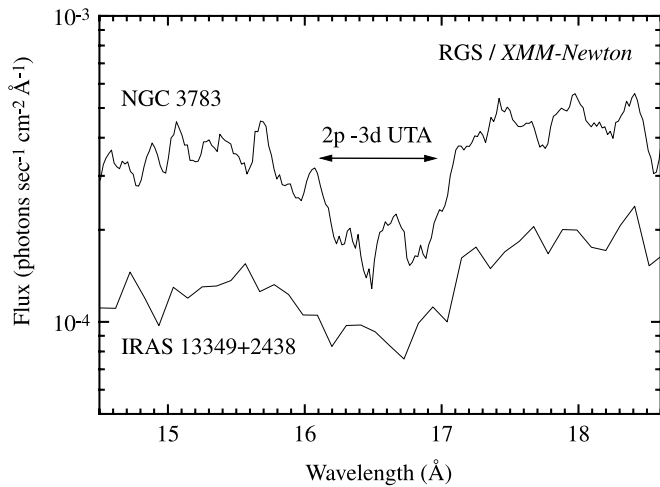


FIG. 1.—RGS spectra of the Seyfert 1 galaxy NGC 3783 and the luminous quasar IRAS 13349 + 2438 featuring a broad trough between 16 and 17 Å, due to numerous inner-shell $n = 2-3$ (mainly $2p-3d$) absorption lines of Fe M-shell ions blended into a UTA.

Photoabsorption from the L-shell ($n = 2$) of neutral (or nearly neutral) Fe falls between 17 and 18 Å. This was most recently detected by Paerels et al. (2001) in the low-mass X-ray binary X0614 + 091. Paerels et al. (2001) mention only the L-shell photoionization edges, probably because of the lack of atomic data for the associated (photoexcitation) lines. Owing to their much higher cross sections, lines should always appear when edges are detected. Thus, in addition to AGN observations, the present calculations are also relevant to spectra produced by absorption of local X-ray sources, such as X0614 + 091, by interstellar Fe in our galaxy. This paper provides an account of the atomic processes and the full details of the spectral modeling issues related to the inner-shell $n = 2-3$ absorption lines of Fe M-shell ions. A compact set of wavelengths and oscillator strengths is made available for fitting this feature to observed spectra and for diagnostics.

2. ATOMIC CALCULATIONS

In order to calculate the wavelengths and oscillator strengths for the radiative transitions, we use the multi-configuration, relativistic HULLAC (Hebrew University Lawrence Livermore Atomic Code) computer package (Bar-Shalom, Klapisch, & Oreg 2001). The intermediate-coupling level energies are calculated using the relativistic version (Luc-Koenig 1972; Klapisch et al. 1977) of the parametric potential method by Klapisch (1971). The relativistic approach employed in HULLAC, which uses the jj coupling scheme for its initial vector basis, is perfectly adequate for the inner-shell excitations studied in this work. The high efficiency of HULLAC is also crucial, owing to the numerous transitions and the considerable complexity of the electronic structure in the ions considered. Calculations are carried out for neutral iron (Fe^{0+}) through Na-like Fe^{15+} . The lower Fe charge states could be less relevant to the AGN vicinity, but more to the narrow-line regions or to X-ray-illuminated interstellar gas.

The atomic structure calculations include the ground configurations $2s^2 2p^6 3l^x$ ($x = 1-14$) for Fe^{15+} through Fe^{2+} , and $2s^2 2p^6 3l^{14} 4s^x$ ($x = 1, 2$) for Fe^{1+} and Fe^{0+} . For the ground configurations of Fe^{1+} and Fe^{0+} , the $[3d + 4s]$ configuration mixings are included, i.e.,

$2s^2 2p^6 3s^2 3p^6 [3d^6 4s^x + 3d^7 4s^{x-1}]$ ($x = 1, 2$). All of the $n = 2-3$ photoexcitation transitions from the ground level are calculated for each ion, among which the $2p-3d$ and $2s-3p$ are the strongest. For charge states Fe^{8+} and lower, the $3p$ subshell is full and, thus, the $2s-3p$ excitation channel is not possible. For Fe^{15+} , the $2p-3s$ excitation channel is open and is also calculated. For the $2p$ -excited $\text{Fe}^{10+}-\text{Fe}^{15+}$ ions, the important $[3s3d + 3p^2]$ configuration mixings are possible and are included, i.e., $2s^2 2p^5 [3s^2 3p^x 3d + 3s3p^{x+2}]$ ($x = 0-4$), as well as $2s^2 2p^5 [3s3d + 3p^2]$ for Fe^{15+} . The significance of other mixing effects, such as $[3p^2 + 3d^2]$, which were found important for excitations out of the $3p$ subshell (Quinet & Hansen 1995), were also examined. We find these mixings to reduce the total $n = 2-3$ photoexcitation effect by about 1% and to alter the level energies by much less than that, while increasing the number of absorption lines by a factor of 10 and more. Therefore, for the sake of simplifying the computations, we have excluded these mixings. Electric and magnetic dipole and quadrupole transitions were computed. The contribution, however, of excitations other than electric dipole is less than 0.1%.

The inner-shell excited levels studied here tend to strongly autoionize. This has several effects on the observed spectrum: first, through the low fluorescence yield. Since the inner-shell $n = 2-3$ photoexcitation processes are by and large followed by autoionization rather than X-ray reemission, they leave an observable imprint only in absorption, but not in emission. This absence of fluorescence following L-shell photoexcitation is evident in the soft X-ray spectra of Seyfert 1 galaxies, but even more so in the Seyfert 2 spectra, where emission is not confused with absorption. The low fluorescence yield further implies that dielectronic recombination via these channels is inefficient. Another consequence of the high autoionization rates is the broad natural widths of the absorption lines associated with inner-shell photoexcitation. At high column densities, the natural width of the line can become important in determining the total flux absorbed. For many of the transitions considered in this work, the total autoionization rate is an order of magnitude higher than the radiative decay rate. Thus, in order to obtain correct line profiles and to account for the total photoabsorption effect, we have calculated the total depletion rate incorporating both the autoionization and radiative decay rates to obtain the natural line width. The natural widths obtained here could be, in some cases, a slight underestimation of the actual width because including all of the autoionization transitions is computationally not permissible. The ionized configurations that were included in the autoionization calculations were the most important ones that can be reached by a single-electron transition from the ground level.

The results of the above-described calculations are shown in Figures 2 and 3, where the absorption spectra produced by the inner-shell $n = 2-3$ excitations are presented for Fe^{0+} through Fe^{15+} . The complex atomic structure and the vast amount of detail in the spectra can be clearly seen in the figures. For display purposes, a low ionic column density of $N_{\text{ion}} = 2 \times 10^{15} \text{ cm}^{-2}$ and a temperature of $kT_{\text{ion}} = 10 \text{ eV}$ are chosen, with no turbulent velocity. These parameter values help minimize the effects of saturation and blending of the individual spectral lines in the plot. The dependence of the observed spectrum on these parameters is discussed below in more detail.

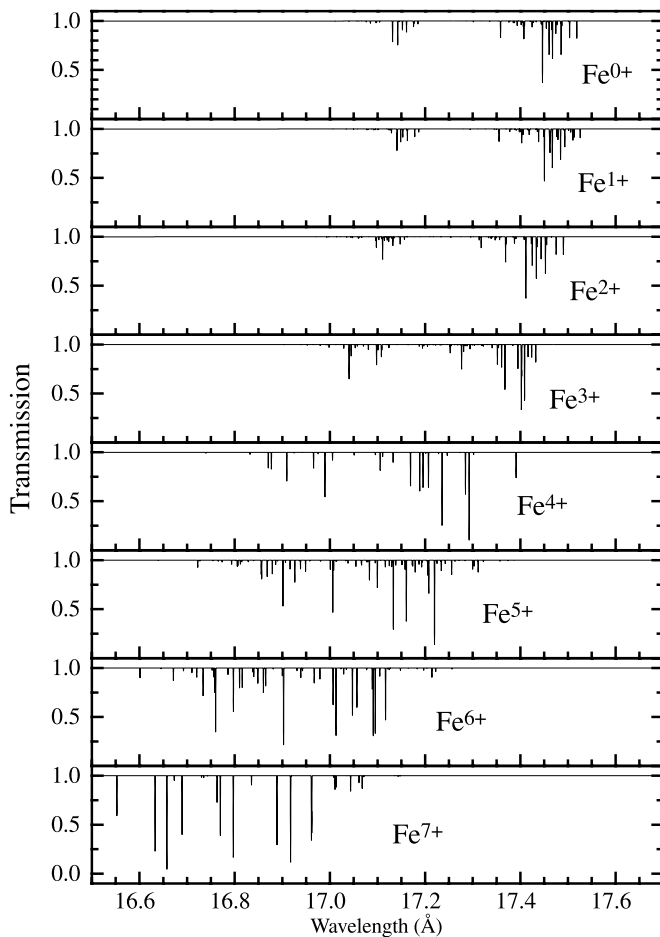


FIG. 2.—Spectra of inner-shell $n=2-3$ absorption lines for Fe^{0+} through Fe^{7+} . A temperature of $kT_{\text{ion}} = 10$ eV and no turbulent velocity are assumed for these plots, in order to minimize line blending and emphasize the complex atomic structure and rich line spectra. The ionic column density used is $2 \times 10^{15} \text{ cm}^{-2}$.

The largest group of lines for each ion represents the $2p-3d$ transition array, which can be seen in the figures to shift from $\sim 17.5 \text{ \AA}$ for Fe^{0+} to $\sim 15.2 \text{ \AA}$ for Fe^{15+} . In fact, the predominant transitions are $2p_{3/2}-3d_{5/2}$ and $2p_{1/2}-3d_{3/2}$. The $2p_{3/2}-3d_{3/2}$ lines are significantly weaker, although mixing among the jj configurations makes it difficult, occasionally, to unambiguously identify a line with a single-electron transition. The observable isonuclear trend of the $2p-3d$ transition array, shifting to shorter wavelengths as the Fe ion charge increases, can be used to accurately diagnose the ionization range of the absorbing plasma. The spectral resolution of the contemporary soft X-ray grating spectrometers on board *Chandra* and *XMM-Newton* are sufficient for measuring the trough of the Fe $2p-3d$ UTA rather precisely. Starting from Fe^{9+} ($\sim 14.9 \text{ \AA}$), where the $3p$ subshell has one vacancy, and continuing to higher charge states ($\sim 14.0 \text{ \AA}$ for Fe^{15+}) with more $3p$ vacancies, the $2s-3p$ lines, mostly $2s-3p_{3/2}$, can also be seen in Figure 3. These lines will usually not be detectable in the spectrum, especially since they overlap with stronger absorption lines that arise from $2p$ excitations to high- n levels (see § 5). Fe^{15+} has also two $2p-3s$ lines calculated at 17.395 and 17.095 \AA , which are not shown in Figure 3.

The present atomic data were compared with results of similar, but partial, calculations by A. J. J. Raassen & J. S. Kaastra (2001, private communication) for several ions in

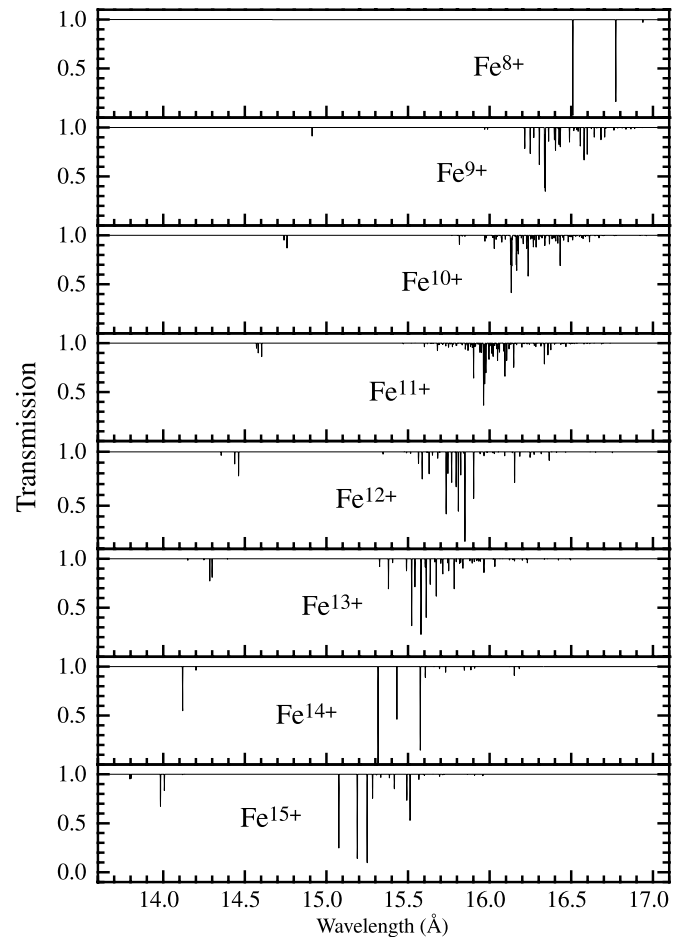


FIG. 3.—Spectra of inner-shell $n=2-3$ absorption lines for Fe^{8+} through Fe^{15+} . A temperature of $kT_{\text{ion}} = 10$ eV and no turbulent velocity are assumed for these plots, in order to minimize line blending and emphasize the complex atomic structure and rich line spectra. The ionic column density used is $2 \times 10^{15} \text{ cm}^{-2}$.

the $\text{Fe}^{6+}-\text{Fe}^{14+}$ range. Raassen & Kaastra used Cowan's atomic code (Cowan 1981), which employs the LS angular momentum coupling scheme with relativistic corrections. The mean wavelengths for individual ions agree to within a few mÅ between the two sets of results. The total oscillator strengths obtained with Cowan's code are systematically higher than the present results. The highest discrepancy of 15% occurs for Fe^{10+} , but for the most part the discrepancies are about 5%–10%. These discrepancies could be explained by Raassen & Kaastra not including the important $[3s3d + 3p^2]$ configuration mixings.

3. SPECTRAL MODELING

The optical depth $\tau(\nu)$ at frequency ν is defined through the exponential attenuation $I(\nu) = I_0(\nu) \exp[-\tau(\nu)]$, where $I_0(\nu)$ and $I(\nu)$ are the unabsorbed and attenuated intensities, respectively.

3.1. Individual Line Absorption

The optical depth $\tau_{ij}(\nu)$ due to an absorption line ($i \rightarrow j$) can be written as

$$\tau_{ij}(\nu) = N_{\text{ion}} \sigma_{ij}(\nu), \quad (1)$$

where N_{ion} is the ionic column density toward the source (in cm^{-2}) and $\sigma_{ij}(\nu)$ is the cross section for photoexcitation (in

cm^2) from i to j . The effect of more than one line at a given frequency is multiplicative (a product of exponents). The photoexcitation cross section is

$$\sigma_{ij}(\nu) = \frac{\pi e^2}{m_e c} f_{ij} \phi(\nu). \quad (2)$$

Here, e and m_e are the electron charge and mass, c is the speed of light, f_{ij} is the line oscillator strength, and $\phi(\nu)$ is the normalized line profile, generally described by a Voigt function, which is the convolution of the (Gaussian) Doppler broadening due to temperature and turbulence and the (Lorentzian) natural width of the line. The Doppler broadening can be characterized by a Doppler width Δv_D :

$$\Delta v_D = \frac{1}{\lambda_{ij}} \sqrt{\frac{2kT_{\text{ion}}}{M_{\text{ion}}} + v_{\text{turb}}^2}, \quad (3)$$

where λ_{ij} is the line wavelength, T_{ion} and M_{ion} are, respectively, the temperature and mass of the absorbing ions, and v_{turb} is the turbulent velocity. Throughout this work we use $kT_{\text{ion}} = 10$ eV. In typical absorbing, photoionized, AGN material, turbulence broadening ($v_{\text{turb}} \geq 100 \text{ km s}^{-1}$) totally dominates over temperature broadening. The natural width Γ_j (in s^{-1}) is associated with the total rate for depletion of the upper level j of the transition:

$$\Gamma_j = \sum_{i' < j} A_{ji'} + \sum_{k' < j} A_{jk'}^a. \quad (4)$$

In the present work, we include both the radiative (A) and autoionization (A^a) rates for determining the natural width.

3.2. Ionization Parameter Zones

Because of the comparable ionization energies of the Fe M-shell ions and the broadband nature of the ionizing flux, in physical photoionized plasmas, several charge states will always be present simultaneously, even if the gas is well confined in space and uniform in density and in temperature. Hence, the observed Fe $2p$ – $3d$ UTA will necessarily be a blend of several charge states. The spectral location and shape of this feature depend on the ionization parameter. We adopt the definition of the ionization parameter, $\xi = L/n_e r^2$, from Tarter, Tucker, & Salpeter (1969), where L is the luminosity of the ionizing source, n_e is the electron density, and r is the distance from the source. The photoabsorption spectra expected for $\xi = 1, 3$, and $10 \text{ ergs s}^{-1} \text{ cm}$ are plotted in Figure 4. The total Fe column density is taken to be $2 \times 10^{17} \text{ cm}^{-2}$, and the ionic fractional abundances are calculated with XSTAR (Kallman & Krolik 1995). The Fe $2p$ – $3d$ UTA can be seen to shift toward shorter wavelengths as ξ increases. The dominant contributions for $\xi = 1, 3$, and $10 \text{ ergs s}^{-1} \text{ cm}$ come, respectively, from Fe^{5+} – Fe^{7+} , Fe^{7+} – Fe^{10+} , and Fe^{10+} – Fe^{13+} . For $\xi = 10 \text{ ergs s}^{-1} \text{ cm}$, the weak $2s$ – $3p$ lines below 15 \AA , which become available for Fe^{9+} and higher charge states, can also be seen in the bottom panel of Figure 4. The Fe $2p$ – $3d$ UTA broadens with ξ as a result of the increasingly larger spacing between charge states for the high-ionization species (see Table 1 in § 4). Despite the various ions partially overlapping in the spectrum, the imprints of individual ions can still be noticed, even for a turbulent velocity of 500 km s^{-1} that was used for Figure 4. Each dip in the theoretical spectra in Figure 4 can be ascribed primarily to one charge state. For the correspondence between (average) wavelength and charge state see Table 1 in § 4. For single- ξ systems with

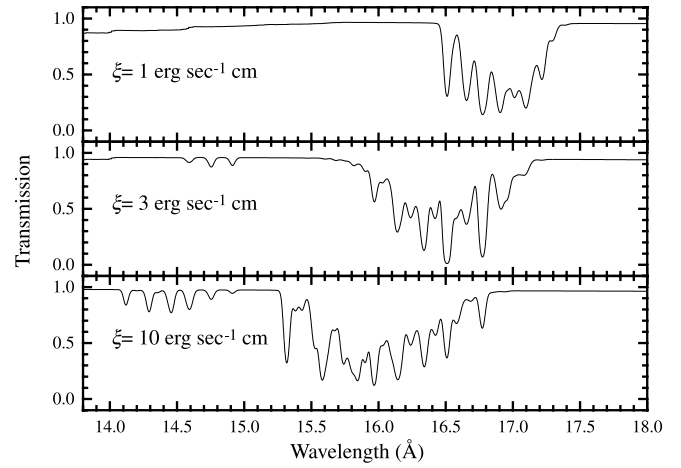


FIG. 4.—Multi-ion spectra featuring numerous inner-shell $n = 2$ – 3 (mainly $2p$ – $3d$) absorption lines of Fe M-shell ions blended into a UTA. Calculations are carried out for single ionization-parameter zones ($\xi = L/n_e r^2$). $N_{\text{Fe}} = 2 \times 10^{17} \text{ cm}^{-2}$ and $v_{\text{turb}} = 500 \text{ km s}^{-1}$ are assumed for the three plots.

comparable velocities ($\leq 700 \text{ km s}^{-1}$), these individual ion contributions could be just marginally resolved. For a detailed analysis of the Fe $2p$ – $3d$ UTA in NGC 3783 and how it breaks up into single-ion contributions, see J. Blustin et al. (2001, in preparation).

Interestingly, all currently known detections of the Fe $2p$ – $3d$ UTA are more or less consistent with a single ionization parameter of $\xi \cong 3 \text{ ergs s}^{-1} \text{ cm}$, while lower and higher ionization states are clearly not observed. In fact, the calculated UTA for $\xi = 3 \text{ ergs s}^{-1} \text{ cm}$ in Figure 4, which falls roughly between 16 and 17 \AA , resembles the observed UTA in both NGC 3783 and IRAS 13349+2438 (see Fig. 1) fairly accurately. Particularly tantalizing is the absence from the soft X-ray spectra of the ions Fe^{12+} – Fe^{15+} , while both lower and higher (Fe-L) charge states show prominent absorption features. This discontinuity in ionization could be indicative of thermal instabilities precluding these ions from coexisting with the adjacent charge states. An investigation of this possibility is beyond the scope of this paper, but preliminary calculations show that thermal instabilities could arise, depending very sensitively on the ionizing spectrum. The absence of charge states lower than Fe^{6+} , on the other hand, is easier to understand, as a consequence of the typical X-ray fluxes in the AGN vicinity, which will instantly ionize a few electrons from the Fe atoms exposed to it. In regions farther out from the center, where ξ could be much lower, the column density through the outflowing and absorbing gas diminishes rapidly and, therefore, it is not observed.

3.3. Equivalent Width

It is customary to assess the total amount of absorption with the equivalent width (EW), which is essentially the area under the (normalized) transmission curve (e.g., Figs. 2 and 3). The EW due to inner-shell $n = 2$ – 3 photoexcitation is plotted in Figure 5 as a function of N_{ion} (the so-called curve of growth) for five selected Fe M-shell ions at $v_{\text{turb}} = 500 \text{ km s}^{-1}$. The EW behavior of these ions represents the EW trend for the other Fe M-shell ions as well. The EW is calculated in the 10 – 20 \AA range only, which is adequate because at the column densities considered for Figure 5, the

TABLE 1
GROUPS OF INNER-SHELL $n = 2-3$ ABSORPTION LINES FROM THE GROUND LEVEL FOR $\text{Fe}^{0+}-\text{Fe}^{15+}$

Ion	Ground Configuration	J_G^a	λ_{av}^b (Å)	Σf_{ij}	Γ_{eff}^c ($\times 10^{14} \text{ s}^{-1}$)	$\Delta\lambda^d$ (Å)	Leading Transition	Number of Lines
Fe^{0+}	$3s^2 3p_{1/2}^2 3p_{3/2}^4 3d_{3/2}^3 3d_{5/2}^3 4s^2$	4	17.453	0.444	3.57	0.037	$2p_{3/2}-3d_{5/2}$	59
			17.142	0.109	3.77	0.025	$2p_{1/2}-3d_{3/2}$	35
Fe^{1+}	$3s^2 3p_{1/2}^2 3p_{3/2}^4 3d_{3/2}^3 3d_{5/2}^3 4s$	9/2	17.457	0.427	3.14	0.037	$2p_{3/2}-3d_{5/2}$	64
			17.148	0.105	3.50	0.027	$2p_{1/2}-3d_{3/2}$	39
Fe^{2+}	$3s^2 3p_{1/2}^2 3p_{3/2}^4 3d_{3/2}^3 3d_{5/2}^3$	4	17.420	0.459	3.45	0.041	$2p_{3/2}-3d_{5/2}$	86
			17.111	0.110	2.90	0.030	$2p_{1/2}-3d_{3/2}$	144
Fe^{3+}	$3s^2 3p_{1/2}^2 3p_{3/2}^4 3d_{3/2}^2 3d_{5/2}^3$	5/2	17.375	0.563	3.18	0.052	$2p_{3/2}-3d_{5/2}$	62
			17.065	0.149	3.24	0.036	$2p_{1/2}-3d_{3/2}$	48
Fe^{4+}	$3s^2 3p_{1/2}^2 3p_{3/2}^4 3d_{3/2}^2 3d_{5/2}^3$	0	17.247	0.769	3.30	0.061	$2p_{3/2}-3d_{5/2}$	17
			16.943	0.191	3.11	0.054	$2p_{1/2}-3d_{3/2}$	15
Fe^{5+}	$3s^2 3p_{1/2}^2 3p_{3/2}^4 3d_{3/2}^3$	3/2	17.179	0.797	2.97	0.056	$2p_{3/2}-3d_{5/2}$	50
			16.918	0.395	2.78	0.073	$2p_{1/2}-3d_{3/2}$	45
Fe^{6+}	$3s^2 3p_{1/2}^2 3p_{3/2}^4 3d_{3/2}^2$	2	17.033	0.988	2.41	0.079	$2p_{3/2}-3d_{5/2}$	45
			16.778	0.481	2.23	0.055	$2p_{1/2}-3d_{3/2}$	23
Fe^{7+}	$3s^2 3p_{1/2}^2 3p_{3/2}^4 3d_{3/2}$	3/2	16.887	1.061	1.66	0.082	$2p_{3/2}-3d_{5/2}$	21
			16.648	0.716	1.95	0.035	$2p_{1/2}-3d_{3/2}$	8
Fe^{8+}	$3s^2 3p_{1/2}^2 3p_{3/2}^4$	0	16.775	0.688	0.96	0.020	$2p_{3/2}-3d_{5/2}$	2
			16.510	1.413	1.72	0.000	$2p_{1/2}-3d_{3/2}$	1
Fe^{9+}	$3s^2 3p_{1/2}^2 3p_{3/2}^3$	3/2	16.614	0.598	0.74	0.074	$2p_{3/2}-3d_{5/2}$	30
			16.337	1.648	1.34	0.070	$2p_{1/2}-3d_{3/2}$	17
Fe^{10+}	$3s^2 3p_{1/2}^2 3p_{3/2}^2$	2	14.912	0.040	3.10	0.000	$2s-3p_{3/2}$	1
			16.472	0.466	0.48	0.090	$2p_{3/2}-3d_{5/2}$	55
Fe^{11+}	$3s^2 3p_{1/2} 3p_{3/2}^2$	3/2	16.159	1.935	1.02	0.089	$2p_{3/2}-3d_{5/2}$	60
			14.754	0.084	2.66	0.008	$2s-3p_{3/2}$	3
Fe^{12+}	$3s^2 3p_{1/2}$	0	16.350	0.309	0.32	0.095	$2p_{3/2}-3d_{5/2}$	61
			15.978	2.239	0.96	0.105	$2p_{1/2}-3d_{3/2}$	90
Fe^{13+}	$3s^2 3p_{1/2}$	1/2	14.591	0.133	2.24	0.014	$2s-3p_{1/2}$	8
			16.209	0.275	0.75	0.118	$2p_{3/2}-3d_{3/2}$	21
Fe^{14+}	$3s^2$	0	15.787	2.418	1.45	0.093	$2p_{3/2}-3d_{5/2}$	27
			14.446	0.178	2.00	0.029	$2s-3p_{3/2}$	4
Fe^{15+}	$3s$	1/2	16.033	0.224	0.78	0.149	$2p_{3/2}-3d_{3/2}$	34
			15.594	2.612	0.84	0.103	$2p_{1/2}-3d_{3/2}$	26
Fe^{16+}	$3s^2$	0	14.288	0.227	1.33	0.028	$2s-3p_{3/2}$	6
			15.622	0.932	0.46	0.137	$2p_{3/2}-3d_{5/2}$	15
Fe^{17+}	$3s^2$	0	15.334	2.063	1.09	0.042	$2p_{1/2}-3d_{3/2}$	2
			14.124	0.282	0.51	0.019	$2s-3p_{3/2}$	2
Fe^{18+}	$3s$	1/2	17.296	0.087	0.03	0.141	$2p_{3/2}-3s$	2
			15.514	0.505	0.35	0.081	$2p_{3/2}-3d_{5/2}$	18
Fe^{19+}	$3s$	1/2	15.191	2.536	0.45	0.072	$2p_{1/2}-3d_{3/2}$	7
			13.966	0.303	0.82	0.068	$2s-3p_{3/2}$	6

^a Total angular momentum quantum number of the ground level.

^b Defined in eq. (5).

^c Defined in eq. (6).

^d Defined in eq. (7).

line wings do not digress much from that region. The EW can be seen to generally increase with the charge state. This is due to the gradual increase in the total oscillator strength with the ionic charge, which, in turn, is mostly attributed to the opening of more and more vacancies in the $n = 3$ shell. No increase in the oscillator strength occurs from Fe^{0+} to Fe^{2+} , because the ground configurations for those ions differ only by their $4s$ shell, which does not affect the $n = 2-3$ excitation. As seen in Figure 5, saturation occurs at about 10^{17} cm^{-2} , except for Fe^{8+} , which has (a closed $3p$ -subshell and thus) only three $2p-3d$ lines (see Fig. 3). The total oscillator strength is concentrated mostly in two of these lines. Consequently, they tend to saturate at lower column densities, as can be seen in Figure 5. Note that at very high column densities, photoexcitation gradually plays a lesser role, since the absorption in photoionization edges (not included in Fig. 5) exceeds that in the lines by far. This effect is discussed further in § 5.

4. ABBREVIATED DATA SET

There are, generally, several dozens of inner-shell $n = 2-3$ lines for each Fe M-shell ion. Typically, 20 lines from each ion account for more than 90% of the EW in typical AGN conditions, with the exception of Fe^{5+} , Fe^{10+} , and Fe^{11+} , where the 20 strongest lines represent a somewhat smaller fraction of that effect. As can be seen in Figures 2 and 3, most of the lines for each ion are concentrated around a narrow spectral region, which can be very close to the corresponding regions for the adjacent charge states. Since several Fe M-shell ions are always present in the plasma simultaneously and since typical AGN turbulent velocities of a few 100 km s^{-1} broaden the spectral lines, the entire ensemble of these lines pertaining to different charge states is coalesced into a broad UTA. This is independent of the spectral resolution of the measuring device. Consequently, the full set of the current atomic data, including its large

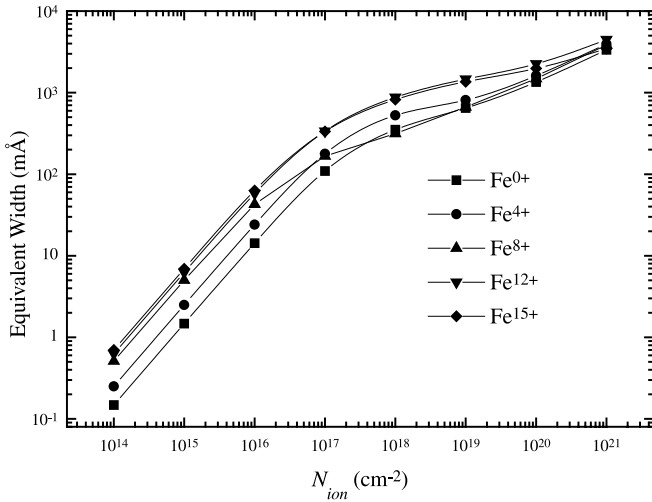


FIG. 5.—Curves of growth for five selected Fe M-shell ions due to the inner-shell $n = 2-3$ (mainly $2p-3d$) absorption lines. EW is calculated in the wavelength region between 10 and 20 Å. v_{turb} is taken to be 500 km s^{-1} .

number of lines for each ion, would in many cases be unnecessary. Alternatively, mean wavelengths and summed oscillator strengths could be adequate for modeling and for spectral fitting purposes.

Bauche-Arnoult, Bauche, & Klapisch (1985) proposed compact formulas for the mean wavelengths and spectral widths of transition arrays. However, since we have already calculated all of the lines level by level, we can simply use our detailed results to obtain these quantities. Additionally, the sum rules in Bauche-Arnoult et al. (1985) do not include the effects of configuration mixing. In order to make the atomic data manageable, we have divided the lines of each charge state into a few groups. Each group is represented by the total oscillator strength of lines in the group $\sum f_{ij}$ and by an f -value averaged wavelength λ_{av} :

$$\lambda_{\text{av}} = \frac{\sum \lambda_{ij} f_{ij}}{\sum f_{ij}}. \quad (5)$$

The sums are carried out over upper levels j , while the lower level i , here, is always the ground level. The effective natural width of a group Γ_{eff} is defined by

$$\Gamma_{\text{eff}} = \frac{\sum \Gamma_j f_{ij}}{\sum f_{ij}}. \quad (6)$$

Each group also has a statistical spectral width $\Delta\lambda$ defined by its f -weighted standard deviation:

$$\Delta\lambda = \sqrt{\frac{\sum (\lambda_{ij} - \lambda_{\text{av}})^2 f_{ij}}{\sum f_{ij}}}. \quad (7)$$

Assuming that the distribution of lines within a group is roughly normal (Gaussian), and for mere modeling purposes, the statistical width can be added to the Doppler width Δv_D as an additional "velocity" component (compare with eq. [3]):

$$\Delta v_D = \frac{1}{\lambda_{ij}} \sqrt{\frac{2kT_{\text{ion}}}{M_{\text{ion}}} + v_{\text{turb}}^2 + 2\left(c \frac{\Delta\lambda}{\lambda_{\text{av}}}\right)^2}. \quad (8)$$

The factor 2 in front of the last term in equation (8) is needed to properly translate $\Delta\lambda$ defined in equation (7) to the usual velocity dependence used for Δv_D .

The groups of $n = 2-3$ absorption lines for Fe M-shell ions in the ground level are listed in Table 1. In the first three columns, the Fe ion is given together with the configuration (in the jj coupling scheme) and total angular momentum quantum number J_G of the ground level. The $n = 1$ and 2 inner electronic shells not specified in the table are assumed to be full. Subsequently, the average wavelength λ_{av} , the total oscillator strength $\sum f_{ij}$, the effective natural width Γ_{eff} (due to autoionization and radiative decay), and the statistical width $\Delta\lambda$, are given for each group. The last two columns in Table 1 indicate the leading radiative transition in the group and the total number of (electric dipole) lines it represents. Both for the highly ionized and for the close-to-neutral species, the separation into groups nicely traces the spin-orbit array splitting discussed in Bauche-Arnoult et al. (1985), where each group can be characterized by a single jj electron transition (e.g., $2p_{1/2}-3d_{3/2}$ and $2p_{3/2}-3d_{5/2}$). For intermediate charge states $\text{Fe}^{10+}-\text{Fe}^{13+}$, where the $[3s3d + 3p^2]$ configuration mixing is strong, the actual atomic levels are often composed of components from more than one configuration, making the single-electron transition identification not absolutely strict. For those ions, the lines do not split as nicely into spin-orbit arrays, as can be seen in Figure 3.

Table 1 shows that the total oscillator strength generally increases with the ionic charge, while the natural width dominated by the total autoionization rates, remains more or less constant. Except for the lowest charge states ($\text{Fe}^{0+}-\text{Fe}^{4+}$), the groups of strong $2p-3d$ lines from each ion are nicely separated by more than 0.1 \AA , easily resolvable with *Chandra* and *XMM-Newton*, enabling an unambiguous measurement of the range of charge states existent in the absorbing plasma. Although the accuracy of the relativistic parametric potential method in HULLAC might slightly diminish as the charge state approaches neutral, for the present inner-shell transitions, these inaccuracies are expected to be much less than 0.1 \AA .

As mentioned above, the statistical widths given in Table 1 facilitate the use of the present atomic data for spectral analysis. We compared the curves of growth obtained with the full atomic data set to those obtained with the abbreviated data set for several cases. The results agree to better than a few percent for N_{ion} up to 10^{16} cm^{-2} (and then again for $N_{\text{ion}} > 10^{19} \text{ cm}^{-2}$). On the other hand, since the largest statistical widths of $\Delta\lambda \sim 0.1 \text{ \AA}$, which occur for the strong groups of $\text{Fe}^{10+}-\text{Fe}^{13+}$, correspond roughly to velocities of 2500 km s^{-1} , for these ions, the abbreviated atomic data set given in Table 1 will reproduce the saturation of the curve of growth correctly only for similarly high velocities. For lower velocities, the shortened method will slightly overestimate the column density at which saturation takes place. In the most extreme cases we checked: $\text{Fe}^{10+}-\text{Fe}^{13+}$ at 100 km s^{-1} , the shortened method can overestimate the actual EW by as much as 40% at a column density of 10^{17} cm^{-2} . For lower charge states or higher velocities, the agreement is much better in the entire range of column densities. In short, although the grouping of lines can be useful for spectral fitting and modeling, the shortened method should be used with caution, particularly for low-velocity systems ($\leq 100 \text{ km s}^{-1}$) and column densities of $10^{17}-10^{18} \text{ cm}^{-2}$.

5. ADDITIONAL AND RELATED ABSORPTION

It is important to note that the present set of calculations is by no means the complete picture for absorption by Fe M-shell ions. The $n = 2-3$ transition array is, indeed, the most conspicuous in the soft X-ray spectrum, but will be regularly accompanied by weaker lines emerging from excitations to higher levels. At high column densities, the photoionization edges could also play a major role. Additionally, even for moderately dense plasmas, the population of ions in excited levels, especially metastable levels, which occasionally lie extremely close in energy to the ground level, can be sufficient to produce photoabsorption from excited levels. This would be due to collisional and photoexcitation as well as radiative cascades toward these levels. In these cases, the absorption spectrum can be calculated only after the excited level populations are determined through comprehensive collisional-radiative models (that include photoexcitation) for each ion.

Full models for all of the ions are beyond the scope of this paper, but we do wish to give an idea of the total photoabsorption effect from the ground level. For this purpose, we choose Fe^{7+} for its relatively simple atomic structure. The absorption spectrum is calculated including inner-shell $2p\text{-}nd$ photoexcitation for $n = 3-9$, as well as the photoionization edges at the $n \rightarrow \infty$ series limit. All these are readily obtained with the HULLAC code. The results are presented in Figure 6 for three ionic column densities of 3×10^{16} , 10^{17} , and 10^{18} cm^{-2} . The latter column density is rarely relevant to AGN sources but nonetheless is used here to exemplify the high-column limit. The turbulent velocity used to calculate the transmission functions in Figure 6 is fixed at 100 km s^{-1} . At a column density of $3 \times 10^{16} \text{ cm}^{-2}$, where the $2p\text{-}3d$ lines are not yet saturated, the high- n lines can be seen to contribute to the absorption spectrum. In fact, the high- n lines can potentially give a sensitive indication of the ionic column density in the region around 10^{17} cm^{-2} , where the $2p\text{-}3d$ UTA is saturated. The photoionization edges, however, although contributing to the EW, are spread out and therefore will be hard to detect. Note the unabsorbed region of the spectrum around 16 \AA between the $2p\text{-}3d$ (UTA) and the $2p\text{-}4d$ features. In the soft X-ray

spectra of many AGNs, but particularly in the spectrum of NGC 3783 where the Fe $2p\text{-}3d$ UTA is deep (J. Blustin et al. 2001, in preparation), the absence of absorption in this region creates a hump that could be mistakenly interpreted as emission. At very high column densities, the photoionization edges dominate the lines as seen in Figure 6. Both the L-shell edges (photoionization from $n = 2$) in the soft X-ray band and the M-shell edges ($n = 3$) that occur at longer wavelengths ($> 50 \text{ \AA}$) can have an appreciable effect on the observed spectrum between 10 and 20 \AA . Both these effects can be seen in the bottom panel of Figure 6 in the high column density plots for $N_{\text{ion}} = 10^{18} \text{ cm}^{-2}$. At these high column densities, even many of the high- n lines are saturated.

In order to quantitatively compare the effect of the $2p\text{-}3d$ UTA with those of the high- n lines as well as with those of the photoionization edges, we plot in Figure 7 the EW as a function of ionic column density, separately for the $2p\text{-}3d$ lines, the $2p\text{-}nd$ ($n = 4-9$) lines, and the L-shell and M-shell photoionization edges. The total EW is also shown. Similarly to Figure 6, the turbulent velocity is fixed at 100 km s^{-1} . It can be seen that up to $N_{\text{ion}} = 10^{17} \text{ cm}^{-2}$, the $2p\text{-}3d$ lines dominate the EW. At higher column densities, when the $2p\text{-}3d$ lines saturate, both the L-shell and M-shell photoionization edges give the predominant absorption effect. The high- n lines give a rather small contribution to the EW, about half that of the $2p\text{-}3d$ lines, although judging from Figure 6, they should be detectable at ionic column densities of $\sim 10^{17} \text{ cm}^{-2}$. These numbers could vary slightly from ion to ion, but the general trends illustrated in Figure 7 are representative of the EW behavior for all of the Fe M-shell ions. For ions, such as Fe^{8+} , in which the $2p\text{-}3d$ lines saturate at lower column densities, the relative contribution of the high- n lines would be more significant.

Note that analogous $2p\text{-}3d$ UTA absorption can also be produced by elements other than Fe. However, in order for those to be observed, many M-shell ions pertaining to those elements need to show high EW in the inner-shell $2p\text{-}3d$ lines, which in turn requires a much lower ionization parameter than that for the Fe $2p\text{-}3d$ UTA. To give a

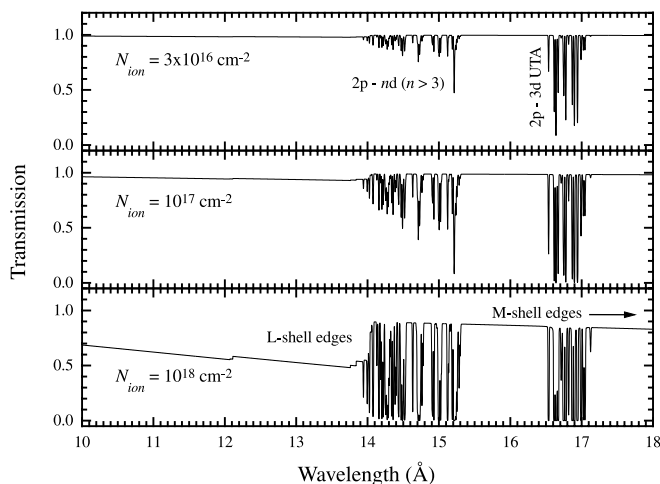


FIG. 6.—Spectra of Fe^{7+} at three different ionic column densities. Calculations include all of the inner-shell $2p\text{-}nd$ ($n = 3-9$) absorption lines, as well as the L-shell and M-shell photoionization edges. The turbulent velocity is fixed at 100 km s^{-1} .

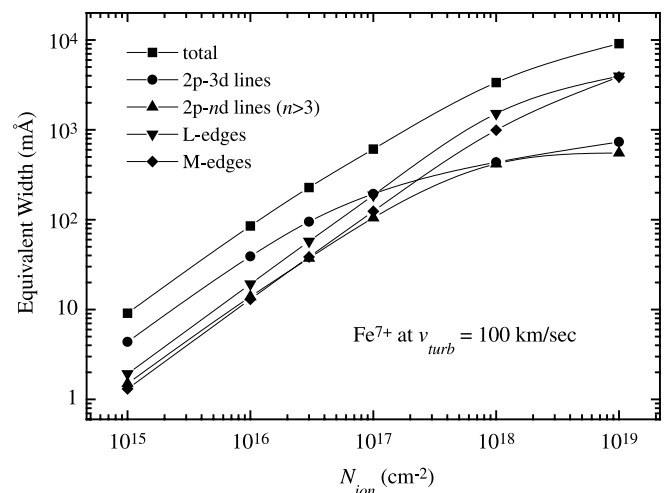


FIG. 7.—Curves of growth for Fe^{7+} . Separate curves are given for the EW contributions of inner-shell $2p\text{-}3d$ absorption lines, inner-shell $2p\text{-}nd$ ($n = 4-9$) absorption lines, and L-shell and M-shell photoionization edges. EW is calculated in the wavelength region between 10 and 20 \AA . v_{turb} is taken to be 100 km s^{-1} .

general idea of where these lines could be expected in the spectrum, we calculated the wavelengths for the strongest inner-shell $2p-3d$ lines of (Mg-like) Ca^{8+} , Ar^{6+} , S^{4+} , and Si^{2+} . The approximate wavelengths are, respectively, 31.4, 43.5, 64.0, and 106 Å. Of these, only the Ca $2p-3d$ UTA falls in the RGS wavelength band, while the others could be observed with the LETG spectrometer on board *Chandra*. In fact, preliminary analysis of the AGN soft X-ray spectra available to us show features that could, tentatively, be identified as inner-shell $2p-3d$ absorption by M-shell Ca. More details will be presented when the analysis is completed.

6. CONCLUSIONS

Extensive calculations for inner-shell $n = 2-3$ (mainly $2p-3d$) photoexcitation have been carried out for neutral iron (Fe^{0+}) and for the 15 ions Fe^{1+} through Fe^{15+} . The corresponding absorption forms a Fe $2p-3d$ UTA that has been observed in AGN spectra between 16 and 17 Å. It is shown that despite strong blending within charge states, the separation (generally greater than 0.1 Å) between the individual ion features enables accurate diagnostics of the ionization range present in the absorbing medium. Ionic column densities of up to about 10^{17} cm^{-2} can be relatively easily diagnosed. Beyond that, the Fe $2p-3d$ UTA will be saturated and other features, such as high- n lines need to be

used. Turbulent velocities of $\leq 700 \text{ km s}^{-1}$ can still be marginally resolved. An abbreviated set of atomic parameters, which can facilitate the spectral modeling of the rather complex Fe $2p-3d$ UTA, is provided and found in most cases to reproduce approximately the EW obtained with the full set of atomic data. Extra caution needs to be applied when using it for low velocities ($\leq 100 \text{ km s}^{-1}$) and ionic column densities of $10^{17}-10^{18} \text{ cm}^{-2}$. Finally, the effects of absorption via $2p-nd$ ($n \geq 4$) lines, which are natural to accompany the $2p-3d$ UTA, should be observable at ionic column densities of $\sim 10^{17} \text{ cm}^{-2}$. Conversely, the spectral signature of the photoionization edges is harder to detect directly, although for ionic column densities of $\sim 10^{17} \text{ cm}^{-2}$ and higher, their contribution to the EW is predicted to exceed that of the lines. Finally, it is pointed out that $2p-3d$ UTA features by lighter elements, such as Ca, Ar, S, and Si, could also be sought in the soft X-ray and EUV spectra of AGNs.

The authors are grateful to the rest of the RGS team for ongoing collaboration, which resulted in the discovery of the Fe $2p-3d$ UTA feature and prompted this work. E. B. acknowledges useful discussions with Marcel Klapisch on the physical properties of UTAs. We acknowledge generous support from the National Aeronautics and Space Administration.

REFERENCES

- Bar-Shalom, A., Klapisch, M., & Oreg, J. 2001, *J. Quant. Spectr. Radiat. Transfer*, 71, 169
 Bauche-Arnoult, C., Bauche, J., & Klapisch, M. 1985, *Phys. Rev. A*, 31, 2248
 Chenais-Popovics, C., et al. 2000, *ApJS*, 127, 275
 Cowan, R. D. 1981, *The Theory of Atomic Structure and Spectra* (Berkeley: Univ. California Press)
 Kallman, T. R. & Krolik, J. H. 1995, XSTAR, A Spectral Analysis Tool (Greenbelt: NASA/GSFC HEASARC)
 Kaspi, S., Brandt, W. N., Netzer, H., Sambruna, R., Chartas, G., Garmire, G. P., & Nousek, J. 2000, *ApJ*, 535, L17
 Kaspi, S., et al. 2001, *ApJ*, 554, 216
 Klapisch, M. 1971, *Comput. Phys. Commun.*, 2, 239
 Klapisch, M., Schwob, J. L., Fraenkel, B., & Oreg, J. 1977, *J. Opt. Soc. Am.*, 67, 148
 Luc-Koenig, E. 1972, *Physica (Utrecht)*, 62, 393
 Paerels, F., et al. 2001, *ApJ*, 546, 338
 Pounds, K., Reeves, J., O'Brien, P., Page, K., Turner M., & Nayakshin, S. 2001, *ApJ*, 559, 181
 Quinet, P., & Hansen, J. E. 1995, *J. Phys. B: At. Mol. Opt. Phys.*, 28, L213
 Sako, M., et al. 2001, *A&A*, 365, L168
 Tarter, C. B., Tucker, W., & Salpeter, E. E. 1969, *ApJ*, 156, 943